



**HAL**  
open science

# Latitudinal Variation of Clouds' Structure Responsible for Venus' Cold Collar

Itziar Garate Lopez, Sébastien Lebonnois

► **To cite this version:**

Itziar Garate Lopez, Sébastien Lebonnois. Latitudinal Variation of Clouds' Structure Responsible for Venus' Cold Collar. *Icarus*, 2018, 10.1016/j.icarus.2018.05.011 . hal-01799821

**HAL Id: hal-01799821**

**<https://hal.sorbonne-universite.fr/hal-01799821>**

Submitted on 25 May 2018

**HAL** is a multi-disciplinary open access archive for the deposit and dissemination of scientific research documents, whether they are published or not. The documents may come from teaching and research institutions in France or abroad, or from public or private research centers.

L'archive ouverte pluridisciplinaire **HAL**, est destinée au dépôt et à la diffusion de documents scientifiques de niveau recherche, publiés ou non, émanant des établissements d'enseignement et de recherche français ou étrangers, des laboratoires publics ou privés.

# Latitudinal Variation of Clouds' Structure Responsible for Venus' Cold Collar

Itziar Garate Lopez <sup>a,\*</sup>, Sébastien Lebonnois <sup>a</sup>

<sup>a</sup>*Laboratoire de Météorologie Dynamique (LMD/IPSL), Sorbonne Universités,  
UPMC Univ Paris 06, ENS, PSL Research University, Ecole Polytechnique,  
Université Paris Saclay, CNRS, Paris, France*

---

## Abstract

Global Climate Models (GCM) are very useful tools to study theoretically the general dynamics and specific phenomena in planetary atmospheres. In the case of Venus, several GCMs succeeded in reproducing the atmosphere's superrotation and the global temperature field. However, the highly variable polar temperature and the permanent cold collar present at  $60^\circ - 80^\circ$  latitude have not been reproduced satisfactorily yet.

Here we improve the radiative transfer scheme of the Institut Pierre Simon Laplace Venus GCM in order to numerically simulate the polar thermal features in Venus atmosphere. The main difference with the previous model is that we now take into account the latitudinal variation of the cloud structure. Both solar heating rates and infrared cooling rates have been modified to consider the cloud top's altitude decrease toward the poles and the variation in latitude of the different particle

modes' abundances.

A new structure that closely resembles the observed cold collar appears in the average temperature field at  $2 \times 10^4 - 4 \times 10^3$  Pa ( $\sim 62 - 66$  km) altitude range and  $60^\circ - 90^\circ$  latitude band. It is not isolated from the pole as in the observation-based maps, but the obtained temperature values (220 K) are in good agreement with observed values. Temperature polar maps across this region show an inner warm region where the polar vortex is observed, but the obtained 230 K average value is colder than the observed mean value and the simulated horizontal structure does not show the fine-scale features present within the vortex.

The comparison with a simulation that does not take into account the latitudinal variation of the cloud structure in the infrared cooling computation, shows that the cloud structure is essential in the cold collar formation. Although our analysis focuses on the improvement of the radiative forcing and the variations it causes in the thermal structure, polar dynamics is definitely affected by this modified environment and a noteworthy upwelling motion is found in the cold collar area.

*Key words:* Venus atmosphere, cold collar, modelling

---

\* Corresponding author.

*Email addresses:* [itziar.garate-lopez@lmd.jussieu.fr](mailto:itziar.garate-lopez@lmd.jussieu.fr) (Itziar Garate Lopez), [sebastien.lebonnois@lmd.jussieu.fr](mailto:sebastien.lebonnois@lmd.jussieu.fr) (Sébastien Lebonnois).

## 1 **1 Introduction**

2 In the last two decades, Global Climate Models (GCMs) have turned out  
3 to be very useful tools to study the general atmospheric circulation on Venus  
4 and the role of different phenomena in the angular momentum budget. Several  
5 numerical simulations by different GCMs have already reproduced the main  
6 characteristic of the Venus atmosphere: its superrotation (e.g. Yamamoto and  
7 Takahashi, 2003; Lee et al., 2007; Sugimoto et al., 2014a; Lebonnois et al.,  
8 2016). At about 70 km altitude clouds circle the solid planet at  $\sim 100$  m/s,  
9 sixty times faster than the rotation of the planet. These simulations sup-  
10 port the Gierasch-Rossow-Williams mechanism (Gierasch, 1975; Rossow and  
11 Williams, 1979) to explain the maintenance of the superrotation, which holds  
12 the latitudinal transport of angular momentum by horizontal planetary-scale  
13 waves and by the meridional circulation responsible for the velocity field in  
14 the atmosphere. GCMs also confirmed that in the case of Venus, the thermal  
15 tides play a key role in transporting the angular momentum vertically (Tak-  
16 agi and Matsuda, 2007; Lebonnois et al., 2010). On the other hand, it is well  
17 known that there is a wide variety of waves in the main cloud deck (Belton  
18 et al., 1976; Rossow et al., 1980; Del Genio and Rossow, 1990; Peralta et al.,  
19 2008; Piccialli et al., 2014) that may contribute to the transport of angular  
20 momentum and, therefore, recent GCMs studies have focused on the analy-  
21 sis of the wave activity present in the Venusian atmosphere (Sugimoto et al.,  
22 2014b; Lebonnois et al., 2016).

23 One of the pending questions for the Venus GCMs is the simulation of the  
24 atmospheric thermal structure. Although the average temperature field has  
25 been reproduced adequately, no model has satisfactorily simulated one of its  
26 most puzzling properties: the polar temperature distribution, formed by highly  
27 variable vortices and cold air areas that surround the vortices permanently  
28 (Zasova et al., 2007; Tellmann et al., 2009).

29 The temperature in the deep atmosphere is almost constant from equa-  
30 tor to around  $50^{\circ}$ , and slowly decreases polewards (Tellmann et al., 2009).  
31 However, above  $\sim 70$  km altitude temperatures increase from equator to pole,  
32 in contrast to what is expected from radiative-convective equilibrium, since  
33 solar heating is higher at equator than at the poles. This is known as the  
34 *warm polar mesosphere*. At 60 - 70 km altitude the temperature field in the  
35  $60^{\circ} - 80^{\circ}$  region has a striking feature in both hemispheres, a strong tem-  
36 perature inversion called the *cold collar* (Taylor et al., 1980). It is a collar  
37 of cold air circling each pole of Venus. The latitudinally averaged tempera-  
38 ture between  $60^{\circ}$  and  $80^{\circ}$  is about 20 K colder than at the equator and 15 K  
39 colder than at the poles, i.e. between  $80^{\circ}$  and  $90^{\circ}$  (Haus et al., 2014). This  
40 temperature difference would cause it to dissipate rapidly, however the cold  
41 collar is a permanent structure at the sub-polar latitudes of Venus, implying  
42 that it is forced by some unknown mechanism. Enclosed by the cold collar  
43 there is a *warm polar vortex* in each pole of Venus. These are rapidly rotat-  
44 ing cloud and temperature structures that show highly variable and complex

45 morphologies with warm small-scale filaments (Piccioni et al., 2007; Luz et al.,  
46 2011; Garate-Lopez et al., 2013). This region features the greatest horizontal  
47 temperature gradient at the cloud top level. Neither the cold collar nor the  
48 warm vortex are completely uniform along the latitude circles (Grassi et al.,  
49 2010; Garate-Lopez et al., 2015); therefore, the latitudinally averaged temper-  
50 ature field hides the real thermal contrast between these two features. The  
51 mean temperature difference between the coldest area of the cold collar and  
52 the warmest nucleus of the vortex is  $\sim 30$  K, but the temperature gradient  
53 can be as high as  $dT/dr = 0.1$  K/km ( $\delta T = 50$  K over 500 km) in this region  
54 (Garate-Lopez et al., 2015).

55 Although these polar structures have been observed repeatedly, their origin  
56 and formation mechanism are still unknown and, therefore, numerical studies  
57 of the Venusian polar region were recently conducted (Yamamoto and Taka-  
58 hashi, 2015; Ando et al., 2016, 2017; Lebonnois et al., 2016). Using GCMs  
59 that force the temperature structure with Newtonian cooling and previously  
60 prepared heating rate profiles, Yamamoto and Takahashi (2015) and Ando  
61 et al. (2016) concluded that thermal tides play an important dynamical role  
62 in the formation of the cold collar and warm vortex. The former stated that  
63 the baroclinic waves are also part of the formation mechanism while the latter  
64 attributed the origin of the polar structures to the combination of the thermal  
65 tides and the residual meridional circulation. Ando et al. (2017) investigated  
66 the vertical structure of the temperature fluctuation in the Venusian polar

67 atmosphere by comparing radio occultation measurements and GCM results,  
68 and concluded that the thermal disturbance associated to the polar vortex  
69 could be a neutral barotropic Rossby wave related to barotropic instability.  
70 These three works obtained a temporally evolving polar region and some hor-  
71 izontal structure within the vortex. However, the average latitude-altitude  
72 distributions of temperature do not exactly reproduce the observed cold col-  
73 lar structure. In observation-based maps (Zasova et al., 2007; Tellmann et al.,  
74 2009; Haus et al., 2014) the cold collar is an isolated region and is located  
75 slightly lower than in the maps of Yamamoto and Takahashi (2015) and Ando  
76 et al. (2016, 2017). In addition, the average temperature values obtained by  
77 Ando et al. (2016) are not warm enough compared to observations.

78 On the other hand, Lebonnois et al. (2016) used the IPSL (Institut Pierre  
79 Simon Laplace) Venus GCM, that has a full radiative transfer module, to  
80 model the Venus atmosphere paying a special attention to polar regions. Their  
81 zonally and temporally averaged latitudinal profiles showed a small cold collar  
82 signature at the cloud top ( $\sim 70$  km), located slightly higher than observed.  
83 Due to its axi-symmetric distribution, the obtained cold collar looked subtle  
84 when zonally averaged but it was more evident in the polar temperature fields.  
85 They related the shape of the polar temperature distribution (cold collar and  
86 warm vortex) to the combination of thermal tide and high-frequency wave ac-  
87 tivity but the temperature contrasts obtained inside the polar regions ( $\sim 10$  K)  
88 were weaker than those presented by Ando et al. (2016, 2017) ( $\sim 20$ -25 K) and

89 were far from the observed  $\sim 30$  K on average (Garate-Lopez et al., 2015).

90 In order to perform an in-depth study of the Venus polar atmosphere and  
91 try to better understand the origin and nature of the cold collar and warm  
92 vortex, we have adapted the IPSL Venus GCM by taking into account the  
93 latitudinal variation of the cloud structure (not considered in any GCM men-  
94 tioned above). The details about the improvements on the radiative transfer  
95 scheme are described in Section 2. Then, Section 3 shows the average temper-  
96 ature and zonal wind fields obtained by the current model, which are in better  
97 agreement with observations and reproduce the characteristic cold collar fea-  
98 ture in a more realistic way than previously. We discuss the formation of the  
99 cold collar in terms of radiative transfer effects in Section 4 and we sum up  
100 the conclusions in Section 5.

## 101 **2 Simulations**

### 102 *2.1 IPSL Venus GCM*

103 The general characteristics of the IPSL Venus GCM have been described in  
104 detail in Lebonnois et al. (2010) and Lebonnois et al. (2016). Therefore, only  
105 a short summary is given here. The model is based on the LMDZ latitude-  
106 longitude grid finite-difference dynamical core (Hourdin et al., 2006). Since  
107 the goal of the current study is the polar regions, it must be noted that this

108 dynamical core includes a longitudinal polar filter: this Fourier filter is applied  
109 at latitudes higher than  $60^\circ$ , removing high frequencies and limiting the ef-  
110 fective resolution to that at  $60^\circ$  latitude (Jablonowski and Williamson, 2011).  
111 Some of the most important features of the model are: the boundary layer  
112 scheme used, based on Mellor and Yamada (1982); the implementation of to-  
113 pography, with hybrid vertical coordinates (50 vertical levels, from surface  
114 to roughly 95 km altitude); the temperature dependence of the specific heat  
115  $C_p(T)$ , which affects the definition of the potential temperature (as detailed  
116 in Lebonnois et al., 2010); and the horizontal resolution currently used, 96  
117 longitudes x 96 latitudes, i.e.  $3.75^\circ \times 1.875^\circ$ .

118 The previous version of the model (Lebonnois et al., 2016) reproduced con-  
119 sistently the average zonal wind and temperature fields, but the obtained  
120 equatorial jet was too intense compared to mid-latitude jets and the winds  
121 below the clouds were too slow compared to measurements made by Venera  
122 and Pioneer Venus probes (Schubert, 1983; Gierasch et al., 1997). On the  
123 other hand, the modeled average temperature structure, although generally  
124 consistent with observations, resulted in colder temperatures in the deep at-  
125 mosphere and at surface compared to observed profiles (Seiff et al., 1985),  
126 and in slightly higher temperatures above the clouds (Tellmann et al., 2009;  
127 Migliorini et al., 2012; Grassi et al., 2014). The latitudinal profiles showed  
128 a small cold collar signature at  $\sim 70$  km and the polar temperature distri-  
129 bution at  $\sim 67$  km displayed some inner structure. However, in the average

130 altitude-latitude temperature map the cold collar was not an isolated feature  
131 as in observation-based maps (Tellmann et al., 2009; Haus et al., 2014) and  
132 the contrast between cold collar and warm vortex was weaker than observed,  
133 about 10 K in the model vs  $\sim 30$  K in temperature retrievals from VIRTIS in-  
134 strument (Garate-Lopez et al., 2015). The latitudinal structure of the clouds  
135 was not taken into account in this previous IPSL model, though Lebonnois  
136 et al. (2016) noted that it could play a role in the shape and strength of the  
137 cold collar.

138 Due to the development of different tools necessary to implement the lati-  
139 tudinal variation of the cloud structure in the solar heating rates and in the  
140 infrared cooling rates, the improvements in the radiative transfer were done  
141 in two stages; (1) implementation of the cloud structure in the solar heating  
142 rates, plus some tuning, and (2) implementation of the cloud structure in the  
143 IR cooling rates (these improvements and tuning are described in the next  
144 section). The simulation started from an already superrotating atmosphere  
145 obtained from previous simulations (Lebonnois et al., 2016) and it was then  
146 run for 200 Venus days (Vd, 117 Earth days) with the partially-improved ra-  
147 diative transfer, the one obtained after the first stage of the improvements.  
148 Two simulations were then pursued for another 100 Vd: one with latitudinally  
149 uniform clouds in the IR cooling computation (referred to as *unifcld* hereon)  
150 and another one with latitudinal variations of the cloud structure for study-  
151 ing the cold collar (*varcld* hereon). The former case, *unifcld* simulation, is

152 used for control by comparing it to the *varcld* simulation in the discussion  
153 of the formation of the cold collar, but this simulation and its results have  
154 no physical sense and should not be considered alone. In the latter case (*var-*  
155 *cld* simulation) a stable state of the atmosphere was obtained after roughly  
156 60 Vd of simulation, so it is the simulation that represents the current IPSL  
157 Venus GCM model. The different inputs used in each stage and simulations  
158 are summarized in Table 1.

## 159 **TABLE 1**

### 160 *2.2 Improved radiative transfer*

161 Previously, the radiative transfer included solar heating rate profiles as a  
162 function of solar zenith angle taken from look-up tables based on Crisp (1986),  
163 and used the infrared net-exchange rate matrix formulation (Eymet et al.,  
164 2009) with horizontally uniform opacity sources (gas and clouds).

165 For the current study, the main modification in the radiative transfer is  
166 related to the cloud model. Our computations now take into account the more  
167 recent cloud model described by Haus et al. (2014, 2015), which is based on  
168 the most recent observations performed by the Venus-Express spacecraft. In  
169 particular, this model describes latitudinal variations of the cloud structure.  
170 According to Haus et al. (2014), the cloud top altitude (defined as the alti-  
171 tude where the optical depth equals the unity at  $1 \mu\text{m}$ ) decreases slowly from

172 about 71 km at the equator to about 70 km at 50°, but then it quickly drops  
173 poleward reaching about 61 km over both poles. Authors also found a strong  
174 latitude dependence of cloud opacity, which is transposed into the latitudinal  
175 behavior of cloud mode factors, scaling the abundance of the different modes  
176 compared to the equatorial vertical distribution. Retrieved mode 1 and 2 fac-  
177 tors gradually decrease poleward of 30° showing a small local minimum at  
178 55°. The mode 3 factor is nearly constant from equator to  $\sim 15^\circ$ , decreases  
179 between 15° and 30°, remains almost constant up to 55°, but then strongly  
180 increases poleward (Haus et al., 2014). This new cloud model and some tuning  
181 (see details below) were implemented both in the solar heating and infrared  
182 cooling rates' computations.

### 183 *2.2.1 Solar heating*

184 For the short-wavelength part of the radiative transfer scheme, the principle  
185 used is basically the same as previously. Look-up tables are used, that contain  
186 the vertical profile of the solar heating rate as a function of solar zenith angle.  
187 The model described in Haus et al. (2015) is now used to produce these tables.  
188 In addition, since the latitudinal structure of the cloud is now taken into  
189 account, the tables vary with latitude, in bins of 5°. It can be noted that in this  
190 cloud model, the unknown ultraviolet absorber is modeled independently from  
191 the cloud particle modes, regardless of the absorber's chemical composition.

192 The vertical profile of the solar heating plays a crucial role in the temper-

193 ature profile, as shown e.g. by Lebonnois et al. (2015). However, it is poorly  
194 constrained by available data. A series of tests were performed with the new  
195 solar heating rates (Lebonnois and Schubert, 2017, Methods and Supplemen-  
196 tary Materials). Below approximately the cloud base, these solar heating rates  
197 are smaller than the ones that were used previously (Crisp, 1986), and this  
198 resulted in deep atmospheric temperature profiles significantly colder than ob-  
199 served. The composition of the lower haze particles, located between the cloud  
200 base (48 km) and 30 km and observed by in-situ probe instruments (Knollen-  
201 berg et al., 1980), is not established, so their optical properties are not well  
202 constrained. This sub-cloud haze is not taken into account in the Haus et al.  
203 (2015) model, except for the tail of the sulfuric acid cloud mode vertical dis-  
204 tributions. The absorption of the solar flux in this region is therefore subject  
205 to uncertainty. To better reproduce the temperature structure in the middle  
206 cloud and below, we decided to increase the solar heating rates in this region,  
207 multiplying the solar heating rates provided by the Haus et al. (2015) model  
208 by a factor of 3. This tuning brings the values in the same range as other  
209 models (Crisp, 1986; Lee and Richardson, 2011), and allows the temperature  
210 profile to reach observed values.

### 211 2.2.2 *Infrared cooling*

212 The long-wavelength part of the radiative transfer scheme is based on the  
213 net-exchange rate (NER) formalism (Eymet et al., 2009). The cloud model

214 (density profile of each mode,  $n_i(z)$ ) used in the previous computation of the  
215 net-exchange rate matrices was from Zasova et al. (2007). In this work, we  
216 now use the cloud model described in Haus et al. (2014). In order to take  
217 into account the latitudinal variations of this model, matrices are computed  
218 for five latitudinal bins:  $0^\circ - 50^\circ$ ,  $50^\circ - 60^\circ$ ,  $60^\circ - 70^\circ$ ,  $70^\circ - 80^\circ$  and  $80^\circ - 90^\circ$ .  
219 When running the GCM, the matrices are interpolated between the central  
220 latitudes of each bin.

221 The gas opacities are computed first for high-resolution spectra, taking into  
222 account updated spectral dataset, Voigt line shape profiles, and a truncation at  
223  $200 \text{ cm}^{-1}$ . Then correlated-k coefficients are computed and used in the NER  
224 matrix calculation. In addition,  $\text{CO}_2$  and  $\text{H}_2\text{O}$  collision-induced absorption  
225 are taken into account, as detailed in Lebonnois et al. (2015). However, as  
226 mentioned in Lebonnois et al. (2015) and Lebonnois and Schubert (2017), it  
227 is difficult to have consistent temperature profiles in the middle and lower  
228 cloud and in the atmosphere below without including some small additional  
229 continuum to close the windows located in the  $[3 - 7] \mu\text{m}$  range, through which  
230 energy is exchanged between the cloud base and the layers just below. Here,  
231 an additional continuum of  $1.3 \times 10^{-6} \text{ cm}^{-1} \text{ amagat}^{-2}$  is taken into account in  
232 the 30 - 48 km region, and  $4 \times 10^{-7} \text{ cm}^{-1} \text{ amagat}^{-2}$  in the 16 - 30 km region,  
233 for a best fit of the VIRA (Seiff et al., 1985) and VeGa-2 (Linkin et al., 1987;  
234 Zasova et al., 2006) temperature profiles (see Lebonnois and Schubert, 2017,  
235 Methods and Supplementary Information).

236 **3 Results**237 *3.1 Average temperature field*

238 As a direct consequence of the above described modifications done in the  
239 radiative transfer (considering both stages), the average temperature field has  
240 significantly improved. The horizontally and temporally averaged tempera-  
241 ture profile is now (*varcld* simulation mentioned above) closer to the VIRA  
242 profile (see Figure 1) with warmer modeled temperatures below the clouds  
243 (and colder above) than in the previous model (Lebonnois et al., 2016). In the  
244 3-dimensional simulations presented here, and compared to the 1-dimensional  
245 tests performed in Lebonnois and Schubert (2017) (Methods and Supplemen-  
246 tary Information), the average temperature field is still approximately 10 K  
247 colder than observed below roughly 70 km. However, due to the sensitivity to  
248 the solar heating rates below the clouds and the associated uncertainties, no  
249 additional tuning was performed.

250 **FIG 1**

251 The altitude-latitude distribution of the zonally and temporally averaged  
252 temperature (Figure 2) shows two clearly differentiated behaviors. Above  $4 \times$   
253  $10^3$  Pa the temperature increases from equator to pole, but below  $2 \times 10^4$  Pa it  
254 smoothly decreases towards the pole, just as seen in observation-based maps  
255 (e.g. Tellmann et al., 2009; Haus et al., 2014). Moreover, a new structure that

256 resembles clearly the cold collar appears for the first time in the IPSL Venus  
257 GCM, at  $2 \times 10^4 - 4 \times 10^3$  Pa ( $\sim 62 - 66$  km) altitude and between  $60^\circ$   
258 and  $90^\circ$  in both hemispheres. This feature is not isolated from the pole as in  
259 the observation-based maps, but it is the most similar feature reproduced so  
260 far. The temperature values obtained with our model ( $\sim 220$  K) are in good  
261 agreement with observations. Therefore, the latitudinal variation of the clouds'  
262 structure plays a key role in the formation of the cold collar. The development  
263 of the cold collar related to the radiative transfer in the polar atmosphere of  
264 Venus is discussed in detail below (Section 4).

## 265 FIG 2

### 266 3.2 Cold collar

267 Figure 3 shows an example of the temperature field at the northern pole at  
268  $7 \times 10^3$  Pa ( $\sim 64$  km) altitude. The atmosphere between  $60^\circ$  and  $85^\circ$  is clearly  
269 colder than the rest of the latitudes, being on average  $\sim 20$  K colder than the  
270 equator and about 10 K colder than the pole. The coldest region seen close  
271 to the terminator shows values about 220 K, in good agreement with values  
272 observed by VIRTIS (e.g. Haus et al., 2014; Garate-Lopez et al., 2015). The  
273 inner warm core shows an average value of 230 K (colder than the observed  
274 mean values). However, we find values as high as 240 K in about 3% of the  
275 time over the last simulated 2 Vd.

276 **FIG 3**

277 The temporal evolution of the polar temperature obtained by our current  
278 model does not always show an inner region surrounded by the cold collar and  
279 the structure simulated within the inner core is smoother than obtained by  
280 Yamamoto and Takahashi (2015) and Ando et al. (2016, 2017) (these GCMs  
281 use spectral dynamical cores that do not have singularities at the pole). The  
282 altitude level where the cold collar is reproduced ( $\sim 64$  km) and the tempera-  
283 ture values ( $\sim 220$  K) obtained by the IPSL Venus GCM are, however, more  
284 consistent with observations (e.g.  $\sim 62$  km and  $\sim 220$  K by Tellmann et al.  
285 2009).

286 The coldest region shows a rotation around the pole with a period of about  
287 5.85 Earth days in the model, that agrees with the 5 - 10 Earth days period  
288 found by (Luz et al., 2011) for the drift of the rotation center of the vor-  
289 tex around the pole. However, the modeled inner core does not show a clear  
290 rotation around the pole, so it is difficult to compare its motion to the one  
291 observed for the warm vortex (Luz et al., 2011; Garate-Lopez et al., 2013).

292 Figure 3 in Lebonnois et al. (2016) displayed four temperature fields at  
293 pressure  $3 \times 10^3$  Pa ( $\sim 67$  km) in the northern polar region that showed a  
294 cold polar region with an inner warmer core. The altitude level where these  
295 features are obtained is slightly different comparing the previous and current  
296 models but the horizontal structure simulated in both cases is very similar in

297 general, probably due to the longitudinal polar filter of the model that does  
298 not allow to reproduce fine-scale features.

### 299 *3.3 Average wind field*

300 Considering the latitudinal structure of the clouds has also improved the  
301 zonally and temporally averaged zonal wind field. The modeled equatorial  
302 jet is now less intense than the mid-latitude jets (Figure 4) as cloud-tracking  
303 measurements suggest (Hueso et al., 2015). The modeled mid-latitude jets are  
304 still located too close to the poles (and, therefore, the latitudinal wind gradient  
305 is still high poleward of  $70^\circ$ ) but their altitude has gone down slightly, while  
306 the equatorial jet has ascended a bit.

### 307 **FIG 4**

308 In the previous model (Lebonnois et al., 2016) winds at 40 - 60 km were  
309 approximately half of the observed values, but the currently modeled winds at  
310 this altitude range are on average  $\sim 20$  m/s (about 75%) faster and are now  
311 in good agreement with the Venera and Pioneer Venus probes' profiles (see  
312 Figure 5). According to a new wave activity analysis that is still on-going work  
313 and will be presented in a subsequent publication, this improvement of the av-  
314 eraged zonal wind could be due to a new baroclinic activity found between 40  
315 and 60 km altitude and that transports heat and angular momentum equator-  
316 wards. Nevertheless, the velocity of the zonal winds below 40 km altitude has

317 decreased showing winds significantly slower than observed, which was not the  
318 case previously. The large-scale gravity waves present in the deep atmosphere  
319 in the previous simulation (Lebonnois et al., 2016) are no longer obtained,  
320 which probably explains this worsening in the zonal wind below 40 km.

321 **FIG 5**

#### 322 4 Cold Collar Analysis

323 To analyze in detail the influence of the latitudinal structure of the clouds in  
324 the formation of the cold collar, the simulation with the latitudinal variations  
325 of the cloud structure (*varcld* simulation) is compared to a control simulation  
326 in which a uniform cloud structure is maintained in the IR cooling computation  
327 (*unifcld* simulation). Note that the simulations differ in the second stage of the  
328 implementation (see Section 2.1), i.e. in the last 100 Vd, so the solar heating  
329 rates take into account the latitudinal variations in both simulations (same  
330 look-up table). The *unifcld* simulation has no physical sense since the cloud  
331 model is different between the solar heating and IR cooling treatments. But  
332 its results are very similar to the previous simulation presented by Lebonnois  
333 et al. (2016), so we think that the comparison between *unifcld* and *varcld*  
334 simulations is useful to identify which are the key elements in the formation  
335 of the cold collar.

336 The cold collar is formed in the *varcld* simulation but not in the *unifcld*

337 simulation, which indicates that the generation of this characteristic feature is  
338 not affected by latitudinal variations of the clouds in the solar heating rates.  
339 It is the influence that the cloud structure has in the IR cooling rates that  
340 forms the cold collar.

341 In the *unifld* simulation (Figure 6a), there is a cold region around  $10^3$  Pa  
342 and  $65^\circ$  that extends downward and poleward, creating a warmer region close  
343 to the pole and above that altitude level, but this cold feature is not exactly  
344 as the one observed (e.g. Tellmann et al., 2009; Haus et al., 2014), it is not  
345 completely surrounded by warmer air. This structure, as well as the global  
346 thermal structure in the *unifld* simulation, is very similar to the structure  
347 obtained in previous works and presented there as the cold collar (Ando et al.,  
348 2016, 2017; Lebonnois et al., 2016). The relation between this structure and  
349 the thermal tides in the polar atmosphere was demonstrated by Ando et al.  
350 (2016) and it should be similar in the *unifld* simulation presented here.

## 351 FIG 6

352 On the other hand, the cold feature seen in the average temperature map  
353 that corresponds to the *varfld* simulation resembles significantly more to the  
354 observed cold collar, being more contrasted from the surrounding warmer at-  
355 mosphere and located at the correct altitude and latitude. It is not completely  
356 isolated which is a characteristic different from observations. It is connected  
357 to the pole at an altitude of about  $10^4$  Pa ( $\sim 62$  km) and then extends upward

358 and equatorward. However, the connection to the pole is most likely related  
359 to the grid used currently in the model which is based on a longitude-latitude  
360 scheme with a longitudinal polar filter that reduces the latitudinal resolution  
361 and removes the high frequency variations in the polar regions. So the results  
362 at latitudes higher than  $80^\circ$  should be taken with caution. A new icosahed-  
363 dral dynamical core (Dubos et al., 2015) will be used in the near future that  
364 should improve the robustness of the computation of the polar circulation.  
365 This should affect the fine structure of the cold collar and the inner warm  
366 core (at about  $4 \times 10^3$  Pa and  $80^\circ - 90^\circ$ ).

367 To confirm the dominant influence of the cloud structure on the IR cooling  
368 and on the temperature field, the IR cooling rates of both *unifcld* and *varcld*  
369 simulations are compared. Figure 7 shows the difference between *varcld* and  
370 *unifcld* IR cooling ( $IR_{varcld} - IR_{unifcld}$ ) at the first timestep of the simulations  
371 after the new cloud model is implemented in the IR cooling computation  
372 ( $0.01 Vd$ ), so that the background temperature field has not changed and is  
373 the same for both simulations, and after  $100 Vd$ , at the end of simulations.  
374 Note that the negative values in Figure 7 mean IR cooling is stronger in  
375 the *varcld* simulation while positive values mean it is stronger in the *unifcld*  
376 simulation. The unit used in the Figure is K/s, so that  $1 \times 10^{-4}$  K/s corresponds  
377 to  $\sim 8.64$  K/Earth day. This is in good agreement with Lee and Richardson  
378 (2011) who states that the IR cooling exceeds 10 K/Ed only above 100 Pa.

379 **FIG 7**

380 From the very first moment when the cloud's latitudinal structure is taken  
381 into account in the IR radiation computation, *unifcld* and *varcld* simulations  
382 evolve in a completely different way with no possible convergence (see Sup-  
383 plementary Material). The atmosphere at the *varcld* simulation develops a  
384 stronger cooling region around  $75^\circ$  latitude and  $10^4$  Pa altitude. It also de-  
385 velops a weaker cooling region around  $85^\circ$  latitude and  $4 \times 10^2$  Pa altitude.  
386 During tens of Venusian days the polar atmosphere evolves in such a way that  
387 after 60 Vd it reaches a new equilibrium, although the average temperature at  
388 the cold collar oscillates slightly afterwards. Figure 7b shows that the stronger  
389 and weaker cooling regions in the *varcld* simulation are still present 40 Vd af-  
390 ter reaching the equilibrium, at 100 Vd. This is important because it means  
391 that the atmosphere at the newly formed cold collar will be constantly cooling  
392 by means of IR radiation in a quite stronger way than the atmosphere above  
393 it (referred to as the warm mesospheric pole hereon). As long as this new  
394 equilibrium endures, the cold collar will remain colder than its surroundings  
395 due to this stronger IR cooling.

396 Figure 8 displays the vertical profile of the IR energy exchange between  
397 different atmospheric levels and space for both *unifcld* and *varcld* simulations  
398 at the end of simulation (100 Vd) and at  $75^\circ$  latitude (cold collar region). The  
399 energy loss to space from the upper clouds ( $\sim 50 - 70$  km altitude) is more  
400 localized in altitude in the *varcld* simulation than in the *unifcld* simulation.  
401 This, as well as the decay rate of the cooling with altitude above the clouds, is

402 inherited from the cloud model by Haus et al. (2014). At high-latitude (higher  
403 than  $60^\circ$ ) the retrieval of the cloud top altitude required the estimation of  
404 another quantity, *the cloud upper altitude boundary*, above which no cloud  
405 particles are considered. This cloud upper altitude boundary (located slightly  
406 above the cloud top defined at  $1 \mu\text{m}$ ) strongly affects the highest peak in  
407 the cooling rates, intensifying it. This peak corresponds mainly to the cooling  
408 rates in the  $6\text{-}12 \mu\text{m}$  range and it is associated to the uppermost layer of cloud  
409 particles in the model. The lowest peak in the vertical profiles of Figure 8  
410 corresponds mostly to the cooling at  $20\text{-}30 \mu\text{m}$  and is associated to the base  
411 of the upper clouds, while the cooling above the clouds occurs mainly in the  
412 aisles of the  $15 \mu\text{m}$  band (Lebonnois et al., 2015).

#### 413 **FIG 8**

414 The position of the cold collar with respect to the cloud top (defined at  
415  $1 \mu\text{m}$ ) and the cloud upper boundary is better seen in Figure 7. It is located  
416 just in between, coinciding with the highest peak of the cooling rates in the  
417 vertical profile. This means that the opacity at  $1 \mu\text{m}$  equals unity within the  
418 upper clouds, but that there is a region with cloud particles above it where the  
419 cold collar is formed. The cold collar is, therefore, located at the uppermost  
420 layer of the clouds. Its position is, however, cloud model dependent since it is  
421 strongly linked to the cloud upper boundary defined by Haus et al. (2014).

422 The induced modifications in the temperature structure affects the circu-

423 lation and the thermal energy transport, both horizontally and vertically. A  
424 detailed analysis of the new dynamical state of the polar atmosphere and  
425 of the transport of heat and angular momentum is beyond the scope of the  
426 present paper, but the tendencies in the temperature fields due to dynamical  
427 heat transport are analyzed here to better understand the new equilibrium  
428 in which the cold collar is formed. This quantity (referred to as dynamical  
429 heating hereon) considers the temperature variations due to the advection by  
430 the mean meridional circulation and due to transient waves. The dynamical  
431 heating/cooling rates in the *varcld* simulation can be seen in Figure 9a. Dy-  
432 namics is globally cooling the low-latitudes and heating the polar regions, as  
433 in the simulation with uniform cloud model and previous simulations (not  
434 shown here). Figure 9b shows the dynamical heating difference between *unif-*  
435 *cld* and *varcld* simulations with positive values meaning stronger heating in  
436 the *varcld* simulation. Not surprisingly, it is the inverse of Figure 7b since  
437 dynamical heating should compensate the radiative cooling in order to have  
438 an atmosphere in thermal equilibrium. Actually, in the cold collar area this  
439 heating due to dynamics is slightly stronger in the *varcld* simulation than in  
440 the *unifcld* simulation to compensate the excess of IR cooling. And in the  
441 warm pole, including the warm mesospheric pole ( $85^\circ$  latitude and  $4 \times 10^2$  Pa)  
442 and the inner warm core ( $85^\circ$  latitude and  $4 \times 10^4$  Pa), the dynamical heating  
443 is weaker due to the weaker IR cooling there.

444 **FIG 9**

445 In Figures 9c and 9d dynamical heating in the *varcld* simulation is sepa-  
446 rated between horizontally and vertically transported heating. In both panels  
447 heating is represented by red colors (positive values) and the cooling due to  
448 dynamics by blue colors (negative values). The atmosphere shows a patchy  
449 structure with dynamical heating and cooling regions interspersed with each  
450 other in both horizontal and vertical terms. These two terms are inversely re-  
451 lated; regions where the horizontal dynamics heats the atmosphere are cooled  
452 by vertical dynamics, and vice versa. However, recall that the effects of taking  
453 into account the latitudinal variations of the clouds take place in the cold col-  
454 lar and warm pole areas (Figure 9b), where dynamics heats the atmosphere  
455 (Figure 9a). Above the clouds, in the warm mesospheric pole, the polar heat-  
456 ing due to dynamics occurs by means of vertical transport (Figure 9d), but  
457 it is mitigated by horizontal transport (Figure 9c). On the other hand, in the  
458 cold collar and inner warm core areas, horizontal transport mostly heats the  
459 area (although a region of dynamical cooling is appreciated between the main  
460 two heating regions). This heating is mitigated by vertical heating transport.

461 Studying the variation of the circulation, particularly of the zonal and  
462 meridional winds, is not trivial due to the high variability present in the po-  
463 lar regions. This study of the horizontal distribution of the dynamical polar  
464 atmosphere in the *varcld* simulation will be presented in a subsequent paper  
465 together with the new wave activity. However, the variation of vertical wind is  
466 interesting and noteworthy. Figure 10 shows the vertical wind velocity fields

467 in both *unifcld* and *varcld* simulations (in Pa/s units, so negative values mean  
468 upwelling motion). Although the main differences take place at the clouds and  
469 levels below, an altered subsidence structure that extends down to 50° lati-  
470 tude is seen in the *varcld* simulation, responsible of the vertical heating seen  
471 in Figure 9d. Ascending air is found in the cold collar between 60° and 70°  
472 latitudes and at about  $10^4$  Pa altitude for the *varcld* simulation which is asso-  
473 ciated with the dynamical cooling seen in Figure 9d. A reversal of the vertical  
474 circulation in the 70° - 90° polar region from *unifcld* to *varcld* simulations is  
475 also clearly seen.

#### 476 **FIG 10**

477 Hence, according to the results of the new IPSL Venus GCM, the cold collar  
478 feature observed in Venus' polar atmosphere is formed by the infrared cooling  
479 region generated by the decrease of the cloud top altitude poleward and the  
480 latitudinal variation of the particles modes. Since the radiative forcing cools  
481 the area while the dynamics heats it, resulting in a region characteristically  
482 cold, it seems that the driver of the cold collar is the radiative transfer rather  
483 than dynamics. However, the presence of the cold collar strongly influences  
484 the dynamics, thus affecting the polar circulation of Venus. Even though the  
485 cloud distribution, radiative transfer, and dynamics form a coupled system in  
486 reality and, therefore, any change in one of the mentioned aspects will bring  
487 along a change in the other aspects, this coupling is not yet present in our  
488 GCM and we can not characterize it in detail.

489 The temporal evolution observed in the modeled polar temperature maps at  
490  $7 \times 10^3$  Pa altitude (not shown here) presents a cold collar that is displaced from  
491 the pole and rotates around it. The obtained rotation period of 5.85 Earth days  
492 agrees with the period found by Luz et al. (2011) for the drift of the rotation  
493 center of the vortex around the pole. This result, together with the structure  
494 of the cold feature in the average temperature field, indicates that the current  
495 IPSL Venus GCM models satisfactorily the subpolar latitudes. However, the  
496 current polar latitudes' treatment is not ideally suited and, therefore, the  
497 modeled inner core does not show neither a clear rotation around the pole nor  
498 detailed horizontal structure within it, as the observed polar vortex does.

## 499 5 Conclusions

500 The previous IPSL Venus GCM (Lebonnois et al., 2016) has been modified  
501 in order to improve the radiative transfer, update the cloud model, and take  
502 into account the latitudinal variation of the clouds (by means of cloud top  
503 altitude and different modes' abundances) in the solar heating profiles and in-  
504 frared cooling computation. The new cloud model used in the current version  
505 is described by Haus et al. (2014) and shows that the cloud top altitude de-  
506 creases towards the pole in Venus's atmosphere and that the different particle  
507 modes' abundances change from equator to pole.

508 The zonally and temporally averaged zonal wind and temperature fields

509 have been improved showing now a better agreement with the observations.  
510 Particularly, the equatorial jet's intensity has decreased compared to the mid-  
511 latitude jets' intensity, the zonal wind velocities between 40 and 60 km altitude  
512 are faster than previously, and the averaged temperature values below (resp.  
513 above) the clouds are now warmer (resp. colder), thus closer to the VIRA  
514 reference profile.

515 The main result, however, is the appearance of a feature in the averaged  
516 altitude-latitude temperature map that resembles the subpolar cold collar ob-  
517 served in Venus's atmosphere. The atmosphere between  $60^\circ$  and  $85^\circ$  shows a  
518 thermal minimum at  $2 \times 10^4 - 4 \times 10^3$  Pa ( $\sim 62 - 66$  km) altitude, being  
519  $\sim 20$  K colder than the equator and about 10 K colder than the pole. The  
520 coldest region shows values about 220 K, in good agreement with observed  
521 values, but the inner warm core shows an average value of 230 K that is colder  
522 than the observed values. The structure simulated within the inner core is  
523 smoother than that obtained by Yamamoto and Takahashi (2015) and Ando  
524 et al. (2016, 2017), but the altitude level where the cold collar is reproduced  
525 and the modeled temperature values are more consistent with observations.

526 According to our analysis the cloud's latitudinal structure is an essential  
527 element in the formation of the cold collar via the IR cooling rates. A strong  
528 cooling region at  $\sim 75^\circ$  and  $10^4$  Pa is developed as soon as the new cloud struc-  
529 ture is implemented in the IR computations and it remains cooling strongly  
530 after a new equilibrium is reached and the cold collar is formed. A region of

531 weak IR cooling is also developed above the polar clouds just where the warm  
532 mesospheric pole is observed.

533 The position of the cold collar is cloud model dependent since it is strongly  
534 linked to the cloud upper altitude boundary (level above which no particles  
535 are considered) defined by Haus et al. (2014) at high latitudes. The IR cooling  
536 peak is located right below this cloud upper boundary, above the cloud top  
537 altitude. This means that the cold collar is located at the uppermost layer  
538 of the clouds, in a region with cloud particles but above the level where the  
539 opacity equals one at  $1 \mu\text{m}$ .

540 Once the atmosphere reaches a new thermal equilibrium, the radiative cool-  
541 ing is compensated by heating due to dynamics. Consequently, the dynamical  
542 heating is stronger at the cold collar area than in the warm mesospheric pole  
543 ( $85^\circ$  and  $4 \times 10^2 \text{ Pa}$ ). Our analysis points to vertical transport (associated to a  
544 subsidence motion that extends down to  $50^\circ$ ) as the main source of dynamical  
545 heating in the warm mesospheric pole and to horizontal transport at the cold  
546 collar.

547 Since the radiative forcing cools the area while the dynamics heats it, re-  
548 sulting in a region characteristically cold, it seems that the driver of the cold  
549 collar is the radiative transfer rather than dynamics.

550 **Acknowledgment**

551 This work was supported by the Centre National d'Etudes Spatiales (CNES).  
552 IGL was supported by CNES postdoc grant. GCM simulations were done at CINES,  
553 France, under the project n°11167. We also thank E. Millour for his technical sup-  
554 port with the model.

ACCEPTED MANUSCRIPT

555 **References**

- 556 Ando, H., Imamura, T., Sugimoto, N., Takagi, M., Kashimura, H., Tellmann,  
557 S., Pätzold, M., Häusler, B., Matsuda, Y., 2017. Vertical structure of the  
558 axi-asymmetric temperature disturbance in the Venusian polar atmosphere:  
559 comparison between radio occultation measurements and GCM results. *J.*  
560 *Geophys. Res. Planets* 122, 1687–1703.
- 561 Ando, H., Sugimoto, N., Takagi, M., Kashimura, H., Imamura, T., Matsuda,  
562 Y., 2016. The puzzling Venusian polar atmospheric structure reproduced by  
563 a general circulation model. *Nature Comm.* 7, 10398.
- 564 Belton, M. J. S., Smith, G. R., Schubert, G., del Genio, A. D., 1976. Cloud  
565 patterns, waves and convection in the Venus atmosphere. *J. Atm. Sci.* 33,  
566 1394–1417.
- 567 Crisp, D., 1986. Radiative forcing of the Venus mesosphere. I - Solar fluxes  
568 and heating rates. *Icarus* 67, 484–514.
- 569 Del Genio, A. D., Rossow, W. B., 1990. Planetary-scale waves and the cyclic  
570 nature of cloud top dynamics on Venus. *J. Atmos. Sci.* 47, 293–318.
- 571 Dubos, T., Dubey, S., Tort, M., Mittal, R., Meurdesoif, Y., Hourdin, F., 2015.  
572 DYNAMICO-1.0, an icosahedral hydrostatic dynamical core designed for  
573 consistency and versatility. *Geosci. Model Dev.* 8, 3131–3150.
- 574 Eymet, V., Fournier, R., Dufresne, J.-L., Lebonnois, S., Hourdin, F., Bullock,  
575 M. A., 2009. Net-exchange parameterization of the thermal infrared radia-  
576 tive transfer in Venus' atmosphere. *J. Geophys. Res.* 114, E11008.

- 577 Garate-Lopez, I., García Muñoz, A., Hueso, R., Sánchez-Lavega, A., 2015. In-  
578 stantaneous three-dimensional thermal structure of the South Polar Vortex  
579 of Venus. *Icarus* 245, 16–31.
- 580 Garate-Lopez, I., Hueso, R., Sánchez-Lavega, A., Peralta, J., Piccioni, G.,  
581 Drossart, P., 2013. A chaotic long-lived vortex at the southern pole of Venus.  
582 *Nature Geosci.* 6, 254–257.
- 583 Gierasch, P., 1975. Meridional circulation and the maintenance of the Venus  
584 atmospheric rotation. *J. Atmos. Sci.* 32, 1038–1044.
- 585 Gierasch, P. J., et al., 1997. The general circulation of the Venus atmosphere:  
586 an assessment. In: S. W. Bougher, D. M. Hunten and R. J. Phillips (Ed.),  
587 *Venus II, geology, geophysics, atmosphere, and solar wind environment.*  
588 Univ. of Arizona Press, pp. 459–500.
- 589 Grassi, D., Migliorini, A., Montabone, L., Lebonnois, S., Cardesin-Moinelo,  
590 A., Piccioni, G., Drossart, P., Zasova, L. V., 2010. The thermal structure of  
591 Venusian night-time mesosphere as observed by VIRTIS-Venus Express. *J.*  
592 *Geophys. Res.* 115, E09007.
- 593 Grassi, D., Politi, R., Ignatiev, N. I., Plainaki, C., Lebonnois, S., Wolkenberg,  
594 P., Montabone, L., Migliorini, A., Piccioni, G., Drossart, P., 2014. The Venus  
595 nighttime atmosphere as observed by VIRTIS-M instrument. Average fields  
596 from the complete infrared data set. *J. Geophys. Res. Planets* 119, 837–849.
- 597 Haus, R., Kappel, D., Arnold, G., 2013. Self-consistent retrieval of tempera-  
598 ture profiles and cloud structure in the northern hemisphere of Venus using  
599 VIRTIS/VEX and PMV VENERA-15 radiation measurements. *Planet. &*

600 Space Sci. 89, 77–101.

601 Haus, R., Kappel, D., Arnold, G., 2014. Atmospheric thermal structure and  
602 cloud features in the southern hemisphere of Venus as retrieved from VIR-  
603 TIS/VEX radiation measurements. *Icarus* 232, 232–248.

604 Haus, R., Kappel, D., Arnold, G., 2015. Radiative heating and cooling in the  
605 middle and lower atmosphere of Venus and responses to atmospheric and  
606 spectroscopic parameter variations. *Planet. & Space Sci.* 117, 262–294.

607 Hourdin, F., Musat, I., Bony, S., Braconnot, P., Codron, F., Dufresne, J.-L.,  
608 Fairhead, L., Filiberti, M.-A., Friedlingstein, P., Grandpeix, J.-Y., Krinner,  
609 G., Levan, P., Li, Z.-X., Lott, F., 2006. The LMDZ4 general circulation  
610 model: climate performance and sensitivity to parameterized physics with  
611 emphasis on tropical convection. *Clim. Dyn.* 27, 787–813.

612 Hueso, R., Peralta, J., Garate-Lopez, I., Bandos, T. V., Sánchez-Lavega, A.,  
613 2015. Six years of Venus winds at the upper cloud level from UV, visible  
614 and near infrared observations from VIRTIS on Venus Express. *Planet. &*  
615 *Space Sci.* 113-114, 78–99.

616 Jablonowski, C., Williamson, D. L., 2011. The pros and cons of diffusion, filters  
617 and fixers in Atmospheric General Circulation Models. In: Lauritzen P. H.,  
618 Jablonowski C., Taylor M. A. and Nair R. D. (Ed.), *Numerical techniques*  
619 *for global atmospheric models*. Springer-Verlag, Berlin Heidelberg, pp. 381–  
620 493.

621 Knollenberg, R. G., Travis, L., Tomasko, M., Smith, P., Ragert, B., Esposito,  
622 L., McCleese, D., Martonchik, J., Beer, R., 1980. The clouds of Venus: A

- 623 synthesis report. *J. Geophys. Res.* 85 (A13), 8059–8081.
- 624 Lebonnois, S., Eymet, V., Lee, C., Vatan d'Ollone, J., 2015. Analysis of the  
625 radiative budget of Venus atmosphere based on infrared Net Exchange Rate  
626 formalism. *J. Geophys. Res. Planets* 120, 1186–1200.
- 627 Lebonnois, S., Hourdin, F., Eymet, V., Crespin, A., Fournier, R., Forget, F.,  
628 2010. Superrotation of Venus' atmosphere analysed with a full General Cir-  
629 culation Model. *J. Geophys. Res.* 115, E06006.
- 630 Lebonnois, S., Schubert, G., 2017. The deep atmosphere of Venus and the  
631 possible role of density-driven separation of CO<sub>2</sub> and N<sub>2</sub>. *Nature Geosci.*  
632 10, 473–477.
- 633 Lebonnois, S., Sugimoto, N., Gilli, G., 2016. Wave analysis in the atmosphere  
634 of Venus below 100-km altitude, simulated by the LMD Venus GCM. *Icarus*  
635 278, 38–51.
- 636 Lee, C., Lewis, S. R., Read, P. L., 2007. Superrotation in a Venus general  
637 circulation model. *J. Geophys. Res.* 112, E04S11.
- 638 Lee, C., Richardson, M. I., 2011. A Discrete Ordinate, Multiple Scattering,  
639 Radiative Transfer Model of the Venus Atmosphere from 0.1 to 260 $\mu$ m. *J.*  
640 *Atm. Sci.* 68, 1323–1339.
- 641 Linkin, V. M., Blamont, J., Deviatkin, S. I., Ignatova, S. P., Kerzhanovich,  
642 V. V., 1987. Thermal structure of the Venus atmosphere according to mea-  
643 surements with the Vega-2 lander. *Kosm. Issled.* 25, 659–672.
- 644 Luz, D., Berry, D. L., Piccioni, G., Drossart, P., Politi, R., Wilson, C. F.,  
645 Erard, S., Nuccilli, F., 2011. Venus's southern polar vortex reveals precessing

- 646 circulation. *Science* 332, 577–.
- 647 Mellor, G. L., Yamada, T., 1982. Development of a turbulent closure model  
648 for geophysical fluid problems. *Rev. Geophys. Space Phys.* 20, 851–875.
- 649 Migliorini, A., Grassi, D., Montabone, L., Lebonnois, S., Drossart, P., Piccioni,  
650 G., 2012. Investigation of air temperature on the nightside of Venus derived  
651 from VIRTIS-H on board Venus-Express. *Icarus* 217, 640–647.
- 652 Peralta, J., Hueso, R., Sanchez-Lavega, A., Piccioni, G., Lanciano, O.,  
653 Drossart, P., 2008. Characterization of mesoscale gravity waves in the upper  
654 and lower clouds of Venus from VEX-VIRTIS images. *J. Geophys. Res.* 113,  
655 E00B18.
- 656 Piccialli, A., Titov, D. V., Sanchez-Lavega, A., Peralta, J., Shalygina, O.,  
657 Markiewicz, W. J., Svedhem, H., 2014. High latitude gravity waves at the  
658 Venus cloud tops as observed by the Venus Monitoring Camera on board  
659 Venus Express. *Icarus* 227, 94–111.
- 660 Piccioni, G., et al., 2007. South-polar features on Venus similar to those near  
661 the north pole. *Nature* 450, 637–640.
- 662 Rossow, W. B., Fels, S. B., Stone, P. H., 1980. Comments on 'A three-  
663 dimensional model of dynamical processes in the Venus atmosphere'. *J.*  
664 *Atmos. Sci.* 37, 250–252.
- 665 Rossow, W. B., Williams, G. P., 1979. Large-scale motion in the Venus' strato-  
666 sphere. *J. Atmos. Sci.* 36, 377–389.
- 667 Schubert, G., 1983. General circulation and the dynamical state of the Venus  
668 atmosphere. In: D. M. Hunten, L. Colin, T. M. Donahue and V. I. Moroz

- 669 (Ed.), Venus. Univ. of Arizona Press, pp. 681–765.
- 670 Seiff, A., Schofield, J. T., Kliore, A. J., et al., 1985. Model of the structure of  
671 the atmosphere of Venus from surface to 100 km altitude. *Adv. Space Res.*  
672 5 (11), 3–58.
- 673 Sugimoto, N., Takagi, M., Matsuda, Y., 2014a. Baroclinic instability in the  
674 Venus atmosphere simulated by GCM. *J. Geophys. Res. Planets* 119, 1950–  
675 1968.
- 676 Sugimoto, N., Takagi, M., Matsuda, Y., 2014b. Waves in a Venus general  
677 circulation model. *Geophys. Res. Lett.* 41, 7461–7467.
- 678 Takagi, M., Matsuda, Y., 2007. Effects of thermal tides on the Venus atmo-  
679 spheric superrotation. *J. Geophys. Res.* 112, D09112.
- 680 Taylor, F. W., et al., 1980. Structure and meteorology of the middle atmo-  
681 sphere of Venus: Infrared remote sounding from the Pioneer Orbiter. *J.*  
682 *Geophys. Res.* 85, 7963–8006.
- 683 Tellmann, S., Pätzold, M., Hausler, B., Bird, M. K., Tyler, G. L., 2009. Struc-  
684 ture of the Venus neutral atmosphere as observed by the radio science ex-  
685 periment VeRa on Venus Express. *J. Geophys. Res.* 114, E00B36.
- 686 Yamamoto, M., Takahashi, M., 2003. The fully developed superrotation sim-  
687 ulated by a General Circulation Model of a Venus-like atmosphere. *J. Atm.*  
688 *Sc.* 60, 561–574.
- 689 Yamamoto, M., Takahashi, M., 2015. Dynamics of polar vortices at cloud top  
690 and base on Venus inferred from a general circulation model: Case of a  
691 strong diurnal thermal tide. *Planet. & Space Sci.* 113, 109–119.

- 692 Zasova, L. V., Ignatiev, N. I., Khatuntsev, I. A., Linkin, V., 2007. Structure  
693 of the Venus atmosphere. *Planet. & Space Sci.* 55, 1712–1728.
- 694 Zasova, L. V., Moroz, V. I., Linkin, V. M., Khatuntsev, I. V., Maiorov, B. S.,  
695 2006. Structure of the Venusian atmosphere from surface up to 100 km.  
696 *Cosmic Res.* 44, 364–383.

ACCEPTED MANUSCRIPT

Table 1  
Chosen inputs for the simulations.

	Solar heating		Correlated-k set		Cloud model (IR)			Continuum (3-7 $\mu$ m)	
	C86 <sup>a</sup>	H15 <sup>b</sup>	L16 <sup>c</sup>	updated	Z07 <sup>d</sup>	H13 <sup>e</sup>	H14 <sup>f</sup>	L16 <sup>c</sup>	updated <sup>g</sup>
Initial state	×		×		×			×	
0-200 Vd		×	×			×			×
200-300 Vd:									
- <i>unifeld</i>		×		×		×			×
- <i>varcl</i>		×		×			×		×

<sup>a</sup> Crisp (1986)

<sup>b</sup> Haus et al. (2015), with additional tuning in lower haze area (see text)

<sup>c</sup> Lebonnois et al. (2016)

<sup>d</sup> Zasova et al. (2007)

<sup>e</sup> Haus et al. (2013), clouds taken as uniform with latitude

<sup>f</sup> Haus et al. (2014), clouds taken as variable with latitude

<sup>g</sup> see text

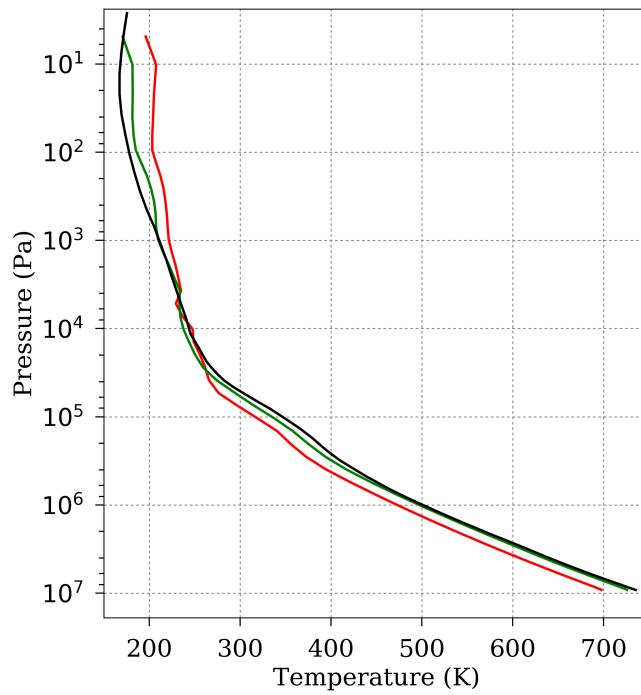


Fig. 1. Horizontally and temporally averaged temperature profile for the previous (red) and current (green) IPSL Venus GCM models at the end of simulation (300 Vd) compared to VIRA reference profile (black). Data is globally averaged over all longitudes and latitudes in each altitude, and over 2 Vd in time.

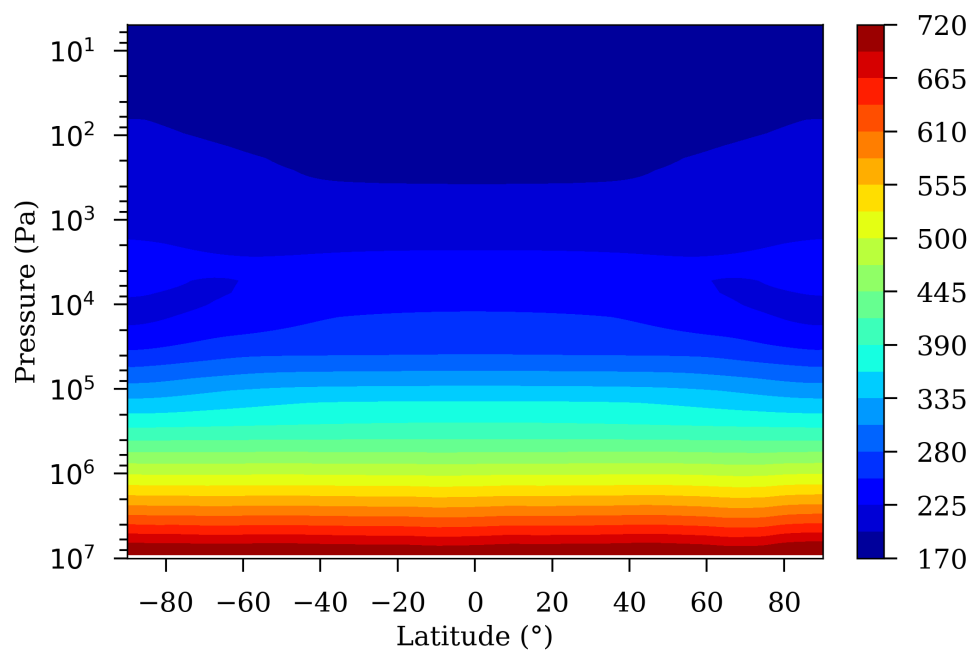


Fig. 2. Zonally and temporally averaged temperature field (K) for the current IPSL Venus GCM model at the end of simulation (300 Vd). Data is averaged over  $360^\circ$  in longitude and 2 Vd in time.

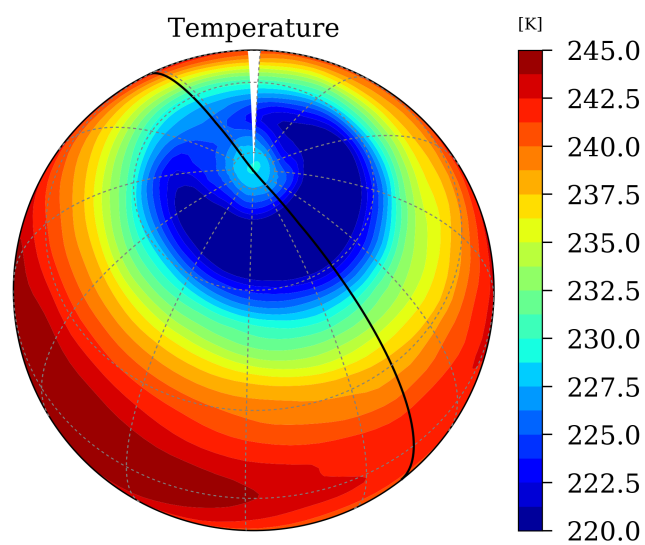


Fig. 3. Example of polar temperature field at  $7 \times 10^3$  Pa ( $\sim 64$  km) for the current IPSL Venus GCM model. Temperature is averaged over  $1/24$  Vd  $\sim 4.88$  Earth days. Black line shows the terminator with dayside on front.

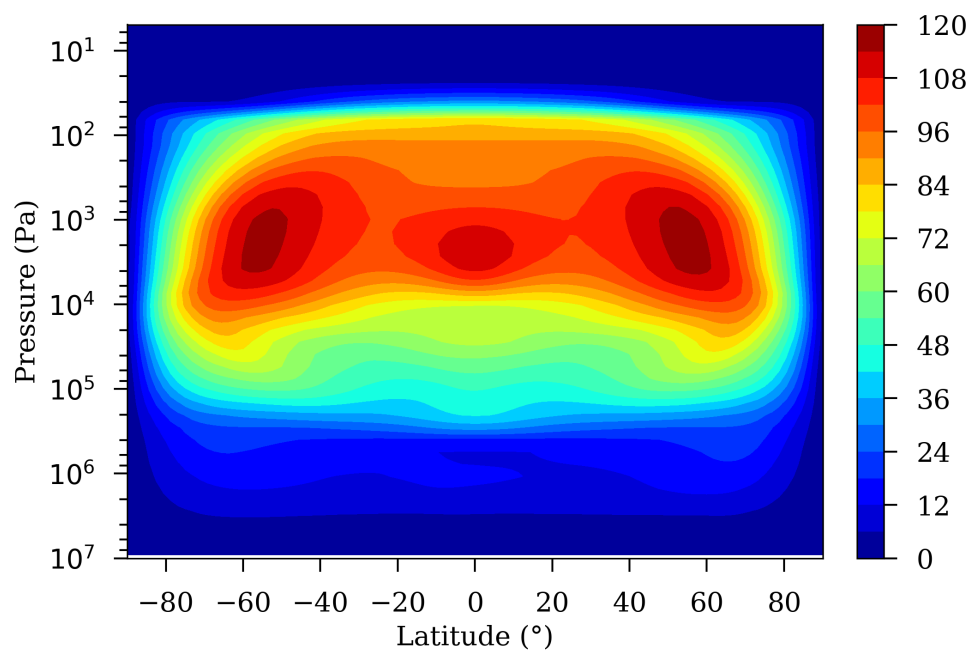


Fig. 4. Zonally and temporally averaged zonal wind field for the current IPSL Venus GCM model at the end of simulation (300 Vd). Data is averaged over  $360^\circ$  in longitude and 2 Vd in time.

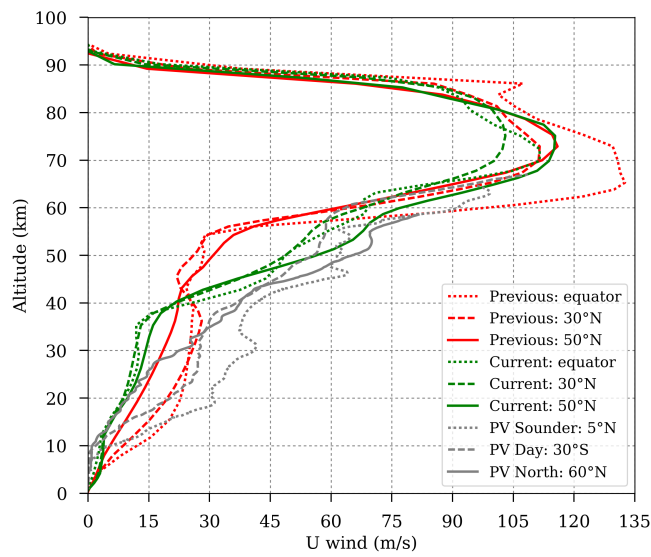


Fig. 5. Vertical profiles of the zonally and temporally averaged zonal wind at different latitudes for the previous (red) and current (green) IPSL Venus GCM models at the end of simulation (300 Vd). Data is averaged over  $360^\circ$  in longitude and 2 Vd in time. Measurements from different Pioneer Venus probes are added in gray.

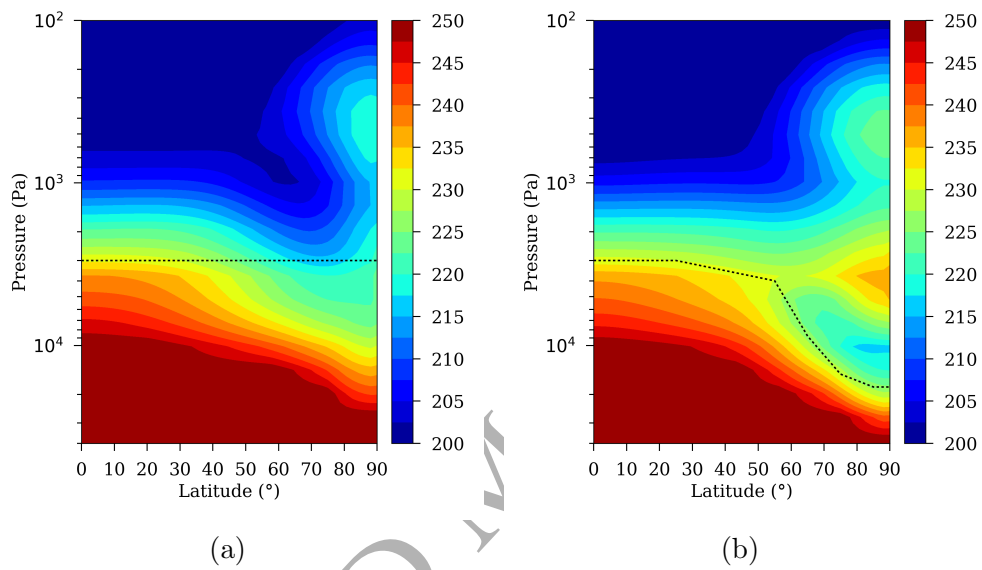


Fig. 6. Zonally and temporally averaged temperature field (K) obtained at the end of simulation (300 Vd) when considering uniform (left) and variable (right) clouds in the IR cooling computation during the last 100 Vd. Data is averaged over  $360^\circ$  in longitude and 2 Vd in time. Dashed line shows the cloud top altitude at  $1 \mu\text{m}$  corresponding to the Haus et al. (2014) cloud model.

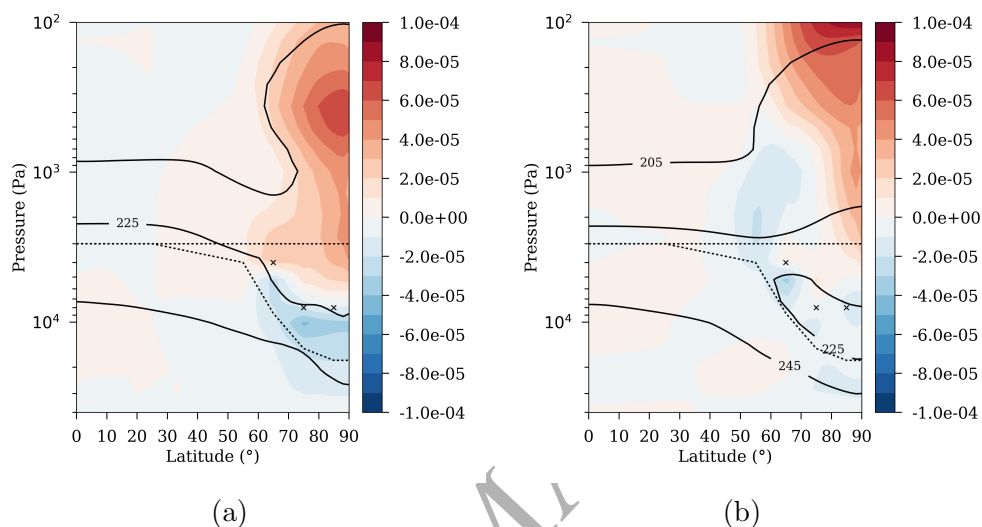


Fig. 7. Difference of the IR cooling rates (K/s) between the *varcld* and *unifcld* simulations as soon as the latitudinal cloud structure is implemented in the IR cooling computation (a, 0.01 Vd, instantaneous field) and 100 Vd after (b, field averaged over 2 Vd). Data is averaged over  $360^\circ$  in longitude. Solid lines show 205K, 225K, and 240K temperature contours of the *varcld* simulation (*unifcld* simulation's temperature field at 0.01 Vd is the same as the *varcld* simulation and 100 Vd after is very similar to that at 0.01 Vd). Dotted lines show the cloud top at  $1 \mu\text{m}$  for the uniform and variable cloud models. Crosses show the cloud upper altitude boundary (see text).

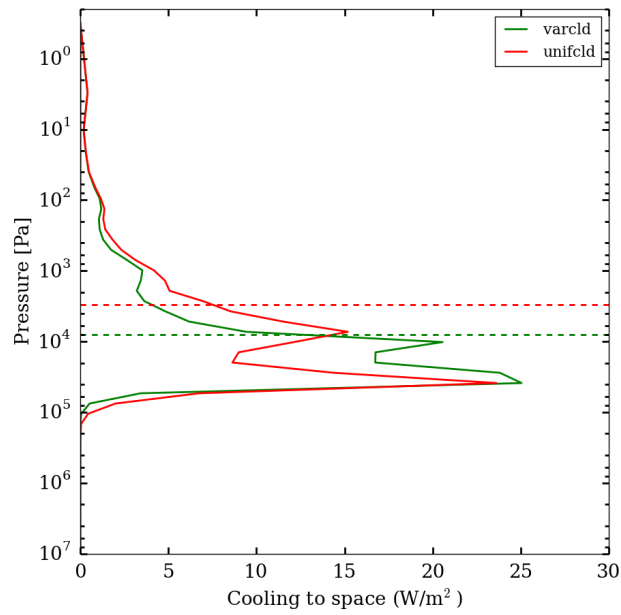


Fig. 8. IR energy exchanges between each layer and space at  $75^\circ$  latitude at the end of simulation (300 Vd, profiles averaged over  $360^\circ$  in longitude and 2 Vd in time) when considering uniform (red, *unifcld*) and variable (green, *varcld*) clouds in the IR cooling computation during the last 100 Vd. Red dashed line indicates the  $1 \mu\text{m}$  cloud-top level in the *unifcld* simulation, while the green dashed line indicates the cloud upper altitude boundary in the *varcld* simulation.

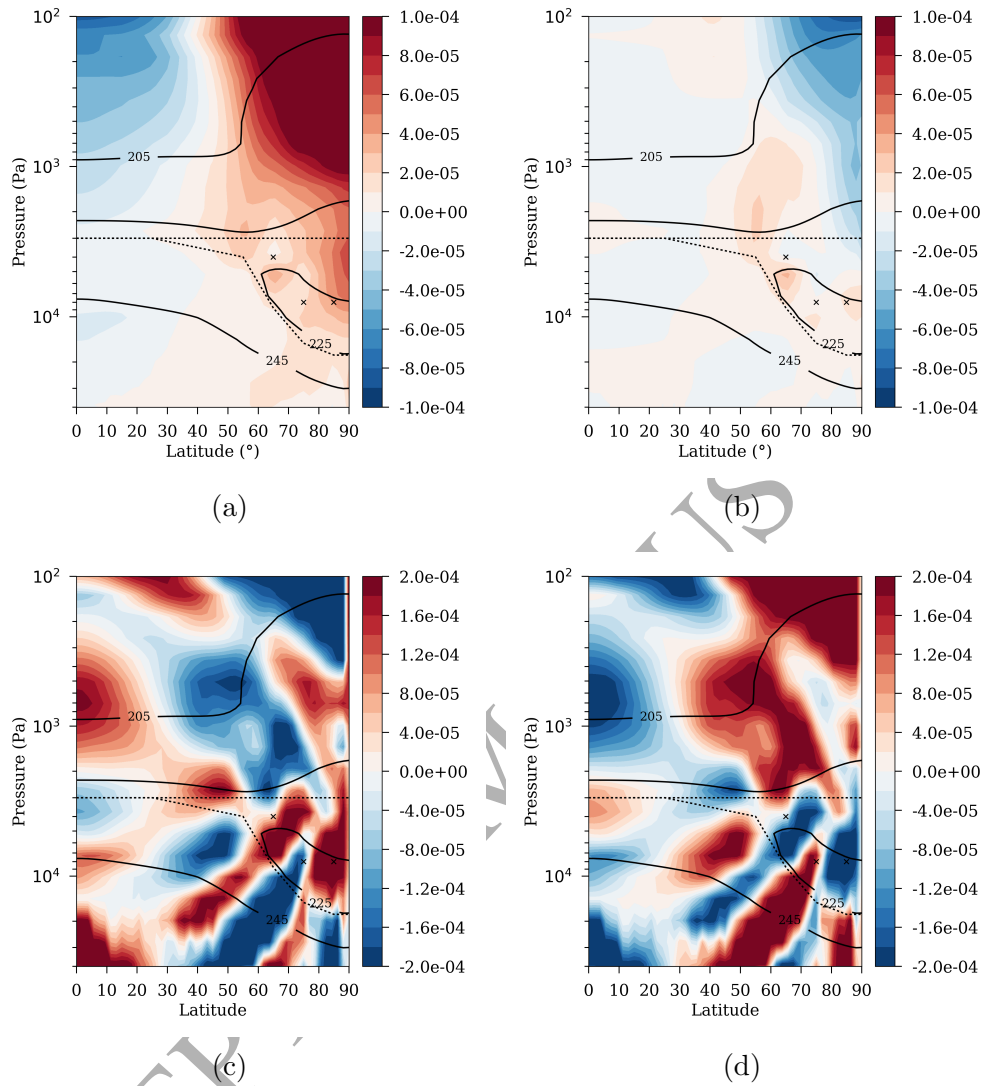


Fig. 9. (a) dynamical heating in the *varcld* simulation, (b) difference of the dynamical heating between *varcld* and *unifcld* simulations, (c) horizontally and (d) vertically transported dynamical heating in the *varcld* simulation. All fields are plotted after 100 Vd with the latitudinal cloud structure implemented (*varcld*) or not (*unifcld*) in the IR cooling computation and are averaged over  $360^\circ$  in longitude and 2 Vd in time. Solid lines, dotted lines and crosses: same as in Fig. 7. Units: K/s.

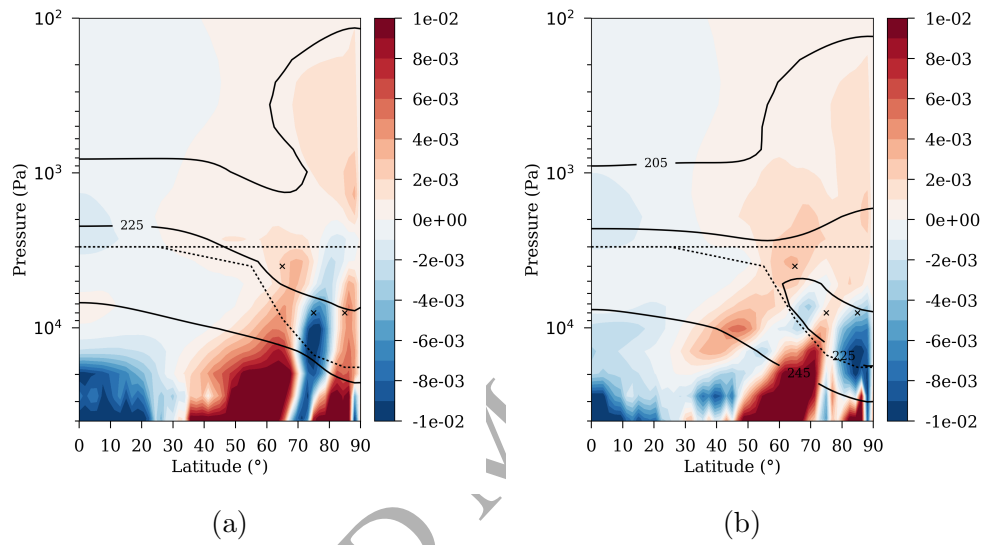


Fig. 10. Zonally and temporally averaged vertical wind velocity (Pa/s) at the end of simulation (300 Vd), when considering uniform (a) and variable (b) clouds in the IR cooling computation during the last 100 Vd. Data is averaged over  $360^\circ$  in longitude and 2 Vd in time. Solid lines, dotted lines and crosses: same as in Fig. 7.